ARTICLE

J. Cent. South Univ. (2019) 26: 1416−1425
DOI: https://doi.org/10.1007/s11771-019-4097-4

Springer

Hydrothermal synthesis and energy storage performance of ultrafine $Ce_2Sn_2O_7$ nanocubes

HUO Yi-feng(霍一峰)[1], QIN Ning(秦宁)[1], LIAO Cheng-zhu(廖成竹)[1], FENG Hui-fen(冯慧芬)[2], GU Ying-ying(古映莹)[2], CHENG Hua(程化)[1]

1. Department of Materials Science and Engineering, Southern University of Science and Technology, Shenzhen 518055, China;
2. Hunan Provincial Key Laboratory of Chemical Power Sources, Hunan Provincial Key Laboratory of Efficient and Clean Utilization of Manganese Resources, College of Chemistry and Chemical Engineering, Central South University, Changsha 410083, China

© Central South University Press and Springer-Verlag GmbH Germany, part of Springer Nature 2019

Abstract: Ultrafine cube-shape $Ce_2Sn_2O_7$ nanoparticles crystallized in pure pyrochlore phase with a size of about 10 nm have been successfully synthesized by a facile hydrothermal method. Conditional experiments have been conducted to optimize the processing parameters including temperature, pH, reaction duration, precipitator types to obtain phase-pure $Ce_2Sn_2O_7$. The crystal structure, morphology and sizes and specific surface area have been characterized by X-ray diffractometer (XRD), Raman spectrum, transmission electron microscope (TEM), high resolution transmission electron microscope (HRTEM), and Brunauer-Emmett-Teller (BET). The as-synthesized $Ce_2Sn_2O_7$ ultrafine nanocubes have been evaluated as electrode materials for pseudo-capacitors and lithium ion batteries. When testing as supercapacitors, a high specific capacitance of 222 F/g at 0.1 A/g and a good cycling stability with a capacitance retention of higher than 86% after 5000 cycle have been achieved. When targeted for anode material for lithium ion batteries, the nanocubes deliver a high specific reversible capacity of more than 900 mA·h/g at 0.05*C* rate. The rate capability and cycling performance is also very promising as compared with the traditional graphite anode.

Key words: supercapacitors; lithium ion batteries; composite oxides; ultrafine nanoparticles; hydrothermal; pyrochlore

Cite this article as: HUO Yi-feng, QIN Ning, LIAO Cheng-zhu, FENG Hui-fen, GU Ying-ying, CHENG Hua. Hydrothermal synthesis and energy storage performance of ultrafine $Ce_2Sn_2O_7$ nanocubes [J]. Journal of Central South University, 2019, 26(6): 1416−1425. DOI: https://doi.org/10.1007/s11771-019-4097-4.

1 Introduction

Supercapacitors with high power capability, stable cycle life, and wide operating temperature range [1, 2] are of great interest for their potential applications in portable electronics, back-up power devices, hybrid electric vehicles, and renewable energy storage systems [3]. Rechargeable lithium ion batteries offer the highest energy density and good cycling performance, which are applied in different fields such as number devices, and cellular phones. Metal oxides, utilizing fast and reversible redox reactions at the surface of active materials, are typical examples of pseudo-capacitive and lithium ion batteries materials, which could

HUO Yi-feng and QIN Ning contributed equally to this work.

Foundation item: Project(JCYJ20170817110251498) supported by the Basic Research Project of the Science and Technology Innovation Commission of Shenzhen, China; Project(2016TQ03C919) supported by the Guangdong Special Support for the Science and Technology Leading Young Scientist, China; Projects(21603094, 21703096) supported by the National Natural Science Foundation of China

Received date: 2018-10-29; **Accepted date:** 2019-02-19

Corresponding author: CHENG Hua, PhD, Associate Professor; Tel: +86-755-88018966; E-mail: chengh@sustc.edu.cn; ORCID: 0000-0002-2656-0343

offer high power and energy density [4]. During the past decade, composite oxides with a formula of $A_2B_2O_7$ have attracted significant attention due to their special thermal, electrical, optical, magnetic, and catalytic properties [5−11], which have wide applications in lithium ion batteries [12], catalysts [13], phosphors [14], ionic conductors [15, 16], and resistance to radiation damage [17]. The extensive application of these complex oxides is closely related to the stability of fluorite and the morphologies and sizes of particles which in turn largely depend on the preparation methods and conditions [18].

There are several reports on the synthesis of $A_2B_2O_7$ composites, such as high temperature solid state reaction [19, 20], coprecipitation [21], hydrothermal [22] and sol-gel [23]. Among these methods, hydrothermal is one of the most simple, practical and cost-effective strategy to synthesize fluorite stannate nanoparticles [18]. There are a couple of examples on the hydrothermal synthesis of phase-pure $Ce_2Sn_2O_7$ [22]. However, to the best of our knowledge, this is the first time to prepare single fluorite phase and cubic shape $Ce_2Sn_2O_7$ ultrafine nanoparticles possessing very high specific surface area and examine it as electrode materials for pseudo-type supercapacitors and anode material for lithium ion batteries. In this work, a facile hydrothermal method was introduced to prepare single fluorite phase $Ce_2Sn_2O_7$ ultrafine nanocubes by changing experimental parameters such as temperature, pH, reaction duration, and precipitators. The optimized synthesis conditions, structure, morphology and electrochemical performance in supercapacitors and lithium ion batteries are studied in detail.

2 Experimental

2.1 Materials preparation

All the reagents were of analytical grade and were used without any further purification. Equal molar of cerium nitrate hydrate ($Ce(NO_3)_3·6H_2O$) and sodium stannate hydrate ($Na_2SnO_3·3H_2O$) were dissolved in deionized water with a total volume of 50 mL under magnetic stirring. Then, different precipitators were dropped into the solution to adjust the pH. After magnetic stirring for 10 min, the mixture was transferred into a teflon-lined stainless steel autoclave of 100 mL capacity and sealed. The autoclave was kept at 150−190 °C for a designed period to examine the influences of the reaction parameters on the crystal structure of final products. After natural cooling, the sample was collected by centrifugation, washed with distilled water for several times, and dried at 60 °C for 24 h in air.

2.2 Materials characterization

Crystallographic phases of the prepared samples were investigated by X-ray diffraction (XRD, Bruker D8 diffractometer with Cu $K_{\alpha 1}$ radiation, λ=1.5406 Å, 40 kV, 250 mA) over a 2θ range from 20° to 90°. The refined structure was obtained by profile matching calculation via Fullprof software. The morphology and size of the sample was examined by transmission electron microscopy (TEM), selected area electron diffraction (SAED) and high resolution transmission electron microscopy (HRTEM) (JEOL-JEM 2010F 200 kV). The specific surface area of the sample was determined by a NOVA 1200e, Quantachrome Instruments in the method of Brunauer–Emmett–Teller (BET) nitrogen adsorption and desorption. Raman spectra were obtained by using a Spex Rama Log 1403 Micro-Raman spectrometer. A green laser (Argon ion laser 514.52 nm) was used with laser power.

2.3 Electrochemical evaluation

To prepare the electrodes for supercapacitor characterization, mixtures with 75 wt% of $Ce_2Sn_2O_7$ nanoparticles, 20 wt% carbon black, and 5 wt% PTFE binder were homogeneously ground in ethanol, which was subsequently brush-coated onto a Ni mesh. The coated mesh was uniaxially pressed to make the active material contact closely with the current collector. Then the mesh was dried at 110 °C in air for 24 h to thoroughly remove the residual solvent and moisture. All the electrochemical characterizations of supercapacitors were carried out in a three-electrode experiment setup with the Ni mesh coated with $Ce_2Sn_2O_7$ as the working electrode, platinum sheet as the counter electrode, saturated calomel electrode (SCE) as the reference electrode, and a 1.0 mol/L Na_2SO_4 aqueous solution as electrolyte. The cyclic voltammetry (CV) and galvanostatic charge−discharge were measured by using an electrochemical workstation (CHI 660D, CH

Instruments, Inc. USA) at room temperature.

The electrochemical testing of the material used as anode of lithium ion battery was performed with 2032-type coin cell, which was assembled in a glove box under dry argon. The electrodes were prepared by 70 wt% $Ce_2Sn_2O_7$ nanoparticles, 20 wt% carbon black, 10 wt% polyvinylidene fluoride binder in N-methylpyrrolidone to form homogeneous slurry. The slurry was spread onto pieces of copper foil. The electrodes were dried at 60 °C at atmospheric pressure for 8 h, and then vacuum-dried for 12 h at 90 °C. The electrolyte was 1 mol/L $LiPF_6$ dissolved in the mixture of 1:1 (by volume) ethylene carbonate (EC) and diethyl carbonate (DEC). Constant-current charge−discharge tests were performed in the range of 0.01−3.00 V using a LAND battery tester at different current densities.

3 Results and discussion

3.1 Preparation of ultrafine $Ce_2Sn_2O_7$ nanocubes

Figure 1 shows the typical XRD pattern as well as the refined profile of the as-synthesized $Ce_2Sn_2O_7$ nanocubes. The corresponding refined factors are as follows: profile residual (R_p), weighted profile R-factor (R_{wp}), expected weighted profile factor (R_{exp}) are processed as 24.8, 22.4 and 15.48, respectively. Brag R-factor and RF-factor are processed as 0.2024 and 0.4463, respectively. A set of reflections centered at 2θ angles of 29.14°, 33.77°, 48.51°, 57.59°, 60.41°, 71.03°, 78.55° and 81.00° are clearly observed, which can be assigned to the (222), (400), (440), (622), (444), (800), (662) and (840) peaks of cubic fluorite $Ce_2Sn_2O_7$ with a space group of *Fd*-3*m*, respectively[19]. The lattice parameter *a* was calculated to be 10.607 (1) Å, a value that is obviously lower than that of the microsized sample prepared by solid-state method (10.6547 Å) [19]. This unit cell contraction can be mainly attributed to the very large surface stress induced by the ultrafine particle size of the as-obtained $Ce_2Sn_2O_7$ nanoparticles with a size of about 10 nm.

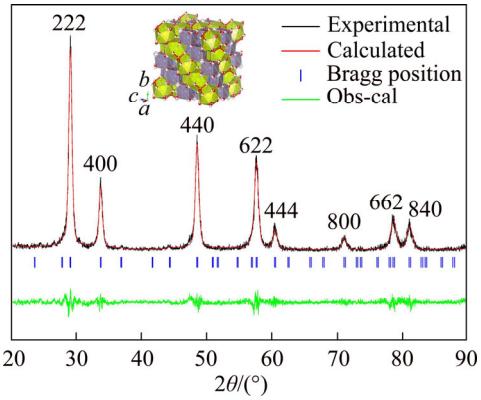

Figure 1 Experimental (black), calculated (red), and powder X-ray diffraction profiles of $Ce_2Sn_2O_7$ nanocubes (Green line is the difference pattern of the refinement; short vertical blue lines are below the profiles mark positions of all position Bragg reflections due to cubic $Ce_2Sn_2O_7$ fluorite. The experimental parameters for synthesizing this sample: 180 ºC, 30 h, pH 12, NaOH)

The effects of hydrothermal temperature on the formation of crystalline $Ce_2Sn_2O_7$ are demonstrated in Figure 2. The precursors prepared at pH 12 were hydrothermally treated for 8 h at different temperatures ranging from 150 to 190 °C using NaOH as precipitators. The product obtained at 150 °C contains small amount of secondary phase of SnO_2 and CeO_2. The impure phase disappears and phase-pure fluorite $Ce_2Sn_2O_7$ was formed when the temperature was higher than 160 °C. However, when the temperature was further raised to 190 °C, impure phase of SnO_2 was observed. From 160 to 190 °C, the diffraction intensity increases and the FWHM decreases with the temperature, an indication of improved crystallinity and growth of particle size at higher temperature.

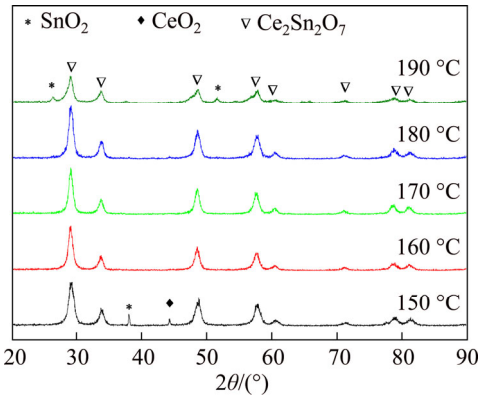

Figure 2 XRD patterns of product prepared with different hydrothermal temperature (Other hydrothermal parameters are constant: pH 12, 8 h, NaOH)

The pH is a key parameter in determining the phase composition of $Ce_2Sn_2O_7$. Generally, with the pH increasing, the solubility of the precursors gradually increased. The XRD pattern in Figure 3 shows that the product produced at pH=8 mainly contained CeO_2 and SnO_2 due to incomplete dissolution of the complex hydrous oxide [22].

When the pH is 9, the diffractions due to $Ce_2Sn_2O_7$ dominate the XRD pattern in addition to small amount of SnO_2. The signals due to SnO_2 become weaker as the increase of pH value, and they totally disappear when the pH is higher than 12. Noticeably, the sample prepared at pH=12 has the highest XRD intensity. Then the XRD intensity reduces as the further increase of pH value. It indicates that in order to obtain single phase $Ce_2Sn_2O_7$, the pH value has to be higher than 12. The sample obtained at pH=12 has the best crystallinity and the further increase of pH value leads to the deterioration of crystallinity and reduction of grain size.

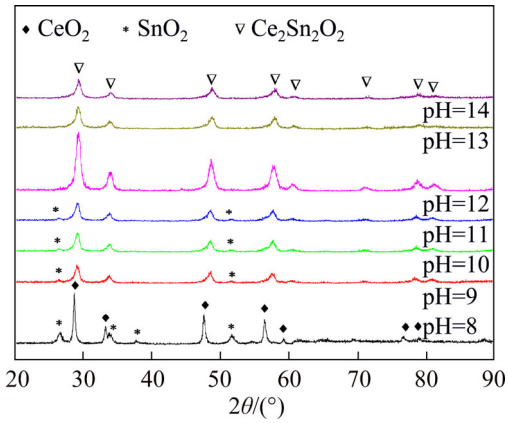

Figure 3 XRD patterns of product prepared with different pH (Other hydrothermal parameters are constant: 180 °C, 8 h, NaOH)

Figure 4 shows the X-ray diffraction patterns of the products as a function of hydrothermal reaction time. It is clear that all the diffraction peaks of the products reacted for 5, 8 and 30 h are in good agreement with phase-pure fluorite $Ce_2Sn_2O_7$. No secondary phases can be observed. Furthermore, as the prolonging of hydrothermal reaction, the diffraction peaks become sharper and narrower, indicating that the crystallinity improves with the reaction time.

The XRD patterns of the product prepared by using NaOH and ammonia solution as precipitators are shown in Figure 5. We can see that phase-pure fluorite $Ce_2Sn_2O_7$ can be obtained either using NaOH or $NH_3·H_2O$. Compared with the sample with $NH_3·H_2O$, the diffraction intensity of that with NaOH was relatively stronger. For the sake of comparison, control experiment has been conducted without using any precipitators. However, it has to be pointed out that the pH of the mixture without

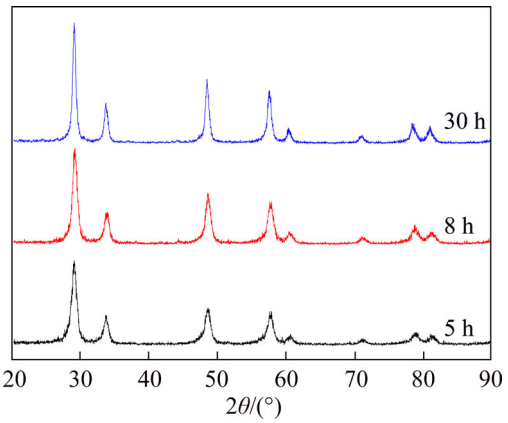

Figure 4 XRD patterns of product prepared with different hydrothermal reaction time (Other experimental parameters are constant: 180 °C, pH 12, NaOH)

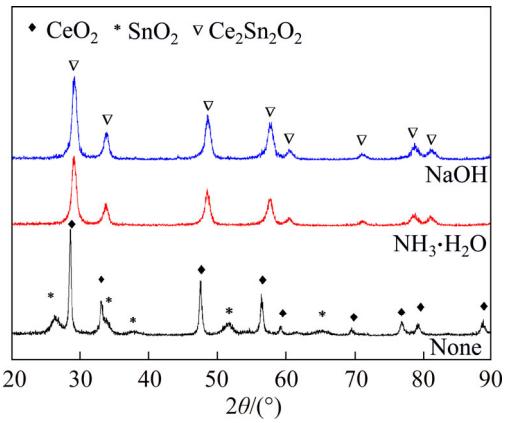

Figure 5 XRD patterns of product prepared with different precipitators (Other hydrothermal parameters are constant: 180 °C, 8 h, pH 12. For comparison, XRD pattern of the sample prepared without using any precipitators is also shown)

adding precipitators was around 8, while pH of the mixtures using NaOH and ammonia was adjusted to be around 12. We can see that without precipitator, two sets of diffractions corresponding to CeO_2 and SnO_2 were clearly observed, and no fluorite $Ce_2Sn_2O_7$ was found.

According to the above results, the possible chemical mechanism for hydrothermal formation of the fluorite $Ce_2Sn_2O_7$ was proposed as follows [24, 25]:

$$SnO_3^{2-}+2H_2O \leftrightarrow H_2SnO_3+2OH^- \quad (1)$$

$$Ce^{3+}+3OH^- \rightarrow Ce(OH)_3\downarrow \quad (2)$$

$$2Ce(OH)_3+2H_2SnO_3 \rightarrow Ce_2Sn_2O_7\downarrow+5H_2O \quad (3)$$

$$H_2SnO_3 \rightarrow SnO_2\downarrow+H_2O \quad (4)$$

$$O_2+4Ce(OH)_3 \rightarrow 4CeO_2\downarrow+6H_2O \quad (5)$$

Owing to the strong hydrolysis effect of Na_2SnO_3, H_2SnO_3 and OH^- were formed under the hydrothermal reaction system as represented in reaction (1). Reaction (2) represents the formation of $Ce(OH)_3$ via reaction between rare-earth ions (Ce^{3+}) and OH^- ions under strong basic condition. Then, during the hydrothermal process, $Ce_2Sn_2O_7$ precipitates were produced from the neutralization reaction between $Ce(OH)_3$ and H_2SnO_3 because the solubility of $Ce_2Sn_2O_7$ was lower than that of $Ce(OH)_3$ under this condition. As shown in reaction (4), SnO_2 nanoparticles were formed when excess H_2SnO_3 existed in the solution. However, the cerium fluorite is hard to be obtained because of the low stability of Ce^{3+} in air. So the precipitate of $Ce(OH)_3$ is easily oxidized to form CeO_2, which is in the valence of 4+ [26].

Figure 6 shows the Raman spectrum of the prepared $Ce_2Sn_2O_7$ nanocubes. We can see that the most intense scattering peak at about 462 cm^{-1} can be ascribed to the F_{1u} mode of Ce−O. At lower wave numbers, there are mainly three modes at around 300, 340, and 397 cm^{-1} that can be attributed to the t_{2g}, E_g, and F_{2g} mode of Ce−O, respectively. The two weak peaks at about 498 and 567 cm^{-1} are due to bending modes of A_{1g} and F_{1u} of Sn−O, respectively [27−31].

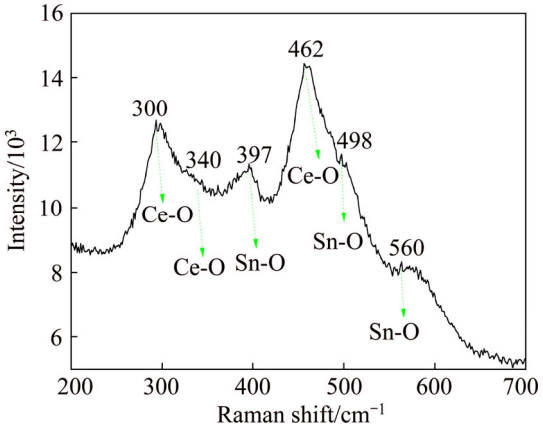

Figure 6 Raman spectrum of $Ce_2Sn_2O_7$ sample hydrothermally treated at 180 °C for 8 h at pH 12 and using NaOH as precipitator

The morphologies and microstructure were investigated by TEM, SAED and HRTEM as shown in Figure 7. The sample demonstrated in Figure 7 was prepared at 180 °C for 8 h, pH 12, and using NaOH as precipitator. As can be seen, well cubic shaped particles with an average edge length of about 10 nm have been obtained. Moreover, the particles are uniform and well dispersed. The SAED pattern shown in inset of Figure 7(a) and HRTEM image shown in Figure 7(b) confirm that the $Ce_2Sn_2O_7$ nanoparticles are well crystallized.

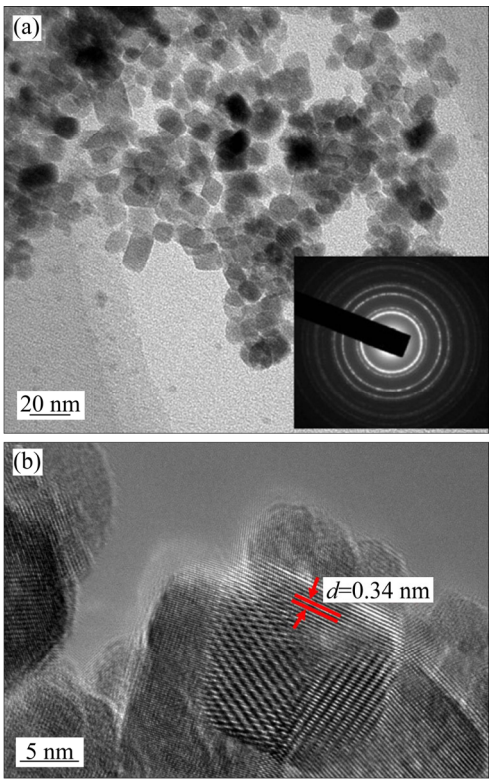

Figure 7 TEM image and corresponding SAED pattern (a) and HRTEM image (b) of sample prepared at 180 °C for 8 h, pH 12 with NaOH

The specific surface area of the prepared $Ce_2Sn_2O_7$ nanocubes was measured under standard temperature and pressure by Brunauer-Emmett-Teller (BET) method. As shown in Figure 8, the N_2 adsorption−desorption isotherm presents an I-type

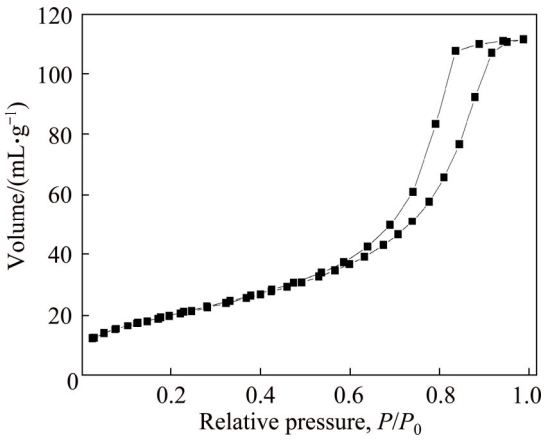

Figure 8 BET adsorption–desorption isotherms of $Ce_2Sn_2O_7$ sample hydrothermally treated at 180 °C for 8 h at pH 12 and using NaOH as precipitator

curve. The specific surface area was about 185.6 m^2/g, which is much higher than that of the samples prepared by the solid-state reaction method with a general vale of 14.1 m^2/g [19, 22]. A high specific surface is highly desirable for the pseudo-capacitive type electrodes that utilize the surface redox reaction. Therefore, high electrochemical activity can be expected from the current ultrafine $Ce_2Sn_2O_7$ nanocubes synthesized by the facile hydrothermal method.

3.2 Pseudo-capacitance performance

Figure 9 shows typical cyclic voltammograms of the supercapacitors by using the as-synthesized $Ce_2Sn_2O_7$ nanocubes as working electrode, Pt as counter electrode, SCE as reference electrode, and 1.0 mol/L Na_2SO_4 aqueous solution as electrolyte at different scan rates. No obvious redox peaks can be found on the CV curves under different scanning rates, indicating that the electrode is charged and discharged at a pseudo-constant rate [32] over the complete voltammetric cycle. The cyclic voltammetry feature in the potential range from −0.8 to −0.3 V is characteristic of a pseudo-capacitive behavior, but it is not perfectly rectangular due to polarization resistance [33]. This effect is noticeably more significant at the less positive potential limit compared to the positive limit. As shown in Figure 9, at slow scan rates, the ions diffused from the electrolyte can access almost all available pores of the electrode. But, when the scan rate increased, the effective interaction between the ions and the electrode is greatly reduced, leading to the deviation of the CV from a rectangular shape.

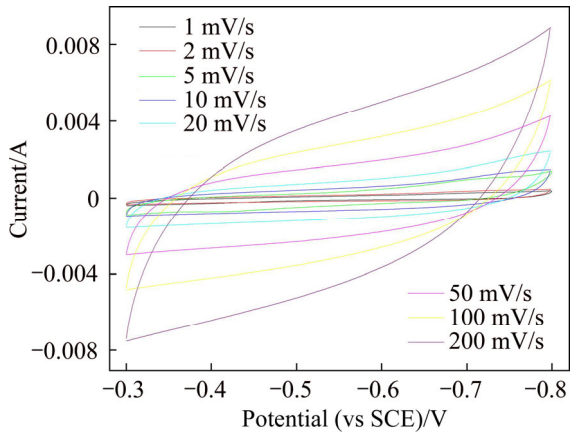

Figure 9 CV curves of $Ce_2Sn_2O_7$ electrode at different scan rates in 1.0 mol/L Na_2SO_4 aqueous electrolyte between −0.8 V and −0.3 V

Figure 10(a) shows the galvanostatic charge−discharge voltage profiles of the nanocubes at a current density of 0.8 A/g. It is clear that the profiles are very symmetric, similar to the typical triangle shape voltage profile of MnO_2 and carbon, which indicates that the as-prepared $Ce_2Sn_2O_7$ nanocubes exhibit excellent pseudo-capacitive characteristics with very good reversibility of surface redox reaction. Figure 10(b) shows the rate performance. The specific capacitance evaluated from the discharge curves was 222, 205, 140, 106, 83, 60 and 48 F/g at the current density of 100, 200, 500, 800, 1000, 1500 and 2000 mA/g, respectively. The capacitance obtained at low rate is better than that of the traditional porous carbon as well as the generally used pseudo-capacitive type electrode materials like MnO_2 and Fe_2O_3. The relatively superior capacitance is mainly attributed to the very high specific surface area of the as-obtained $Ce_2Sn_2O_7$ ultrafine nanocubes. However, the specific capacitance has a quick decrease with the

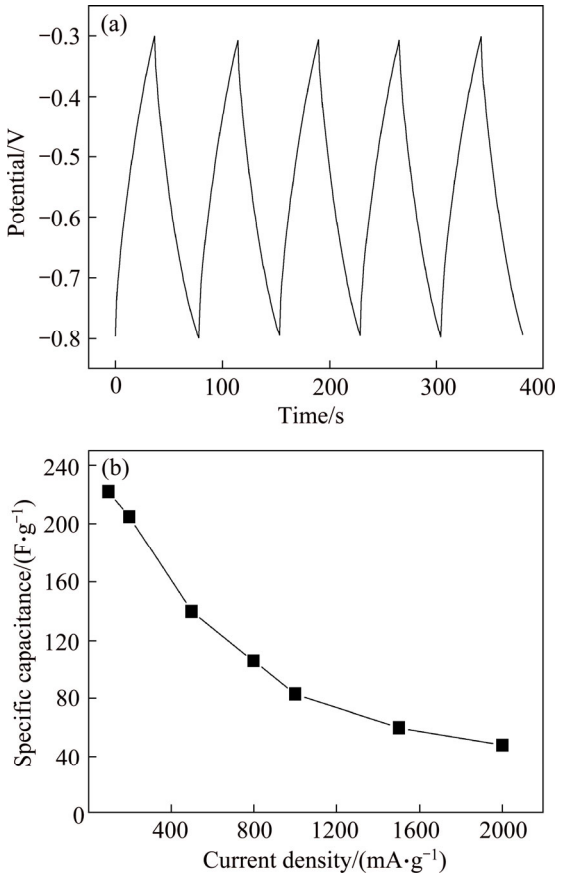

Figure 10 Galvanostatic charge−discharge curves of electrode at current density of 800 mA/g (a) and specific capacitance of $Ce_2Sn_2O_7$ electrode at different current densities (b) in 1.0 mol/L Na_2SO_4 aqueous electrolyte between −0.8 V and −0.3 V

increasing current densities. The reason is predominantly due to the low electronic conductivity of the as-produced $Ce_2Sn_2O_7$ ultrafine nanocubes without conductive carbon coating.

Figure 11 shows the cycling performance at a current density of 100 mA/g in 1.0 mol/L Na_2SO_4 aqueous electrolyte between −0.8 and −0.3 V. After 5000 continuous cycles at the current density of 100 mA/g, the specific capacitance of $Ce_2Sn_2O_7$ electrode decreases slightly from 222 to 191 F/g, with a capacitance retention of more than 86%. It indicates that the as-prepared $Ce_2Sn_2O_7$ ultrafine nanocubes demonstrate very stable pseudo-capacitive cycling performance.

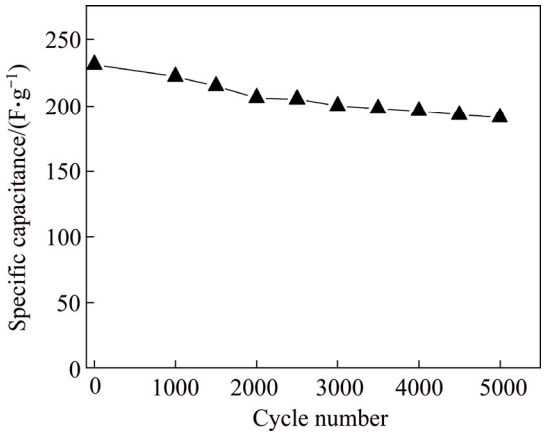

Figure 11 Cycling performance of $Ce_2Sn_2O_7$ electrode at current density of 100 mA/g in 1.0 mol/L Na_2SO_4 aqueous electrolyte between −0.8 V and −0.3 V

Based on the previous report [33−37], a mechanisms was proposed for the charge storage in $Ce_2Sn_2O_7$ electrodes.

$$Ce_2Sn_2O_7+Na^++e^-\leftrightarrow Ce_2Sn_2O_7Na \quad (6)$$

$$(Ce_2Sn_2O_7)_{surface}+Na^+\leftrightarrow(Ce_2Sn_2O_7)Na^+{}_{surface} \quad (7)$$

Reaction (6) implies the intercalation of alkali metal cations Na^+ in the electrode during reduction and deintercalation upon oxidation. The charge stores is reasonably attributed to the proton diffusion into the nanocomposites during the charge storage and release process, accompanying the III/IV oxidation state change of Sn at or near the surface of $Ce_2Sn_2O_7$ nanostructures [33−36]. This is responsible for a relatively higher specific capacitance at a lower scan rate as compared with that at high scan rates. Reaction (7) corresponds to the adsorption of cations (Na^+) in the electrolyte on the very surface of ultrafine $Ce_2Sn_2O_7$ nanocubes. This mechanism was proposed following the observation of significant difference of the cyclic voltammogram and the capacitance of $Ce_2Sn_2O_7$ [37]. It is believed that the electrode capacitance depends primarily on the crystalline structure as well as the morphology and particle size of the active materials, particularly on the specific surface area. The ultrafine cube-shape $Ce_2Sn_2O_7$ nanoparticles provide a relatively easy and quick path for electronic and ion transport, and the large specific surface area considerably improves the accessible active sites for redox faradic reactions, facilitating enhanced capacitance.

3.3 Lithium-ion battery performance

Figure 12(a) displays the 2nd cycle charge−discharge curves of $Ce_2Sn_2O_7$ electrode at different current density ranging from 0.05*C* to 20*C*. All the curves show slopping charge discharge voltage profiles in the range of 0−3 V. The reversible charge capacity at the current density of 0.05*C*, 0.1*C*, 0.5*C*,

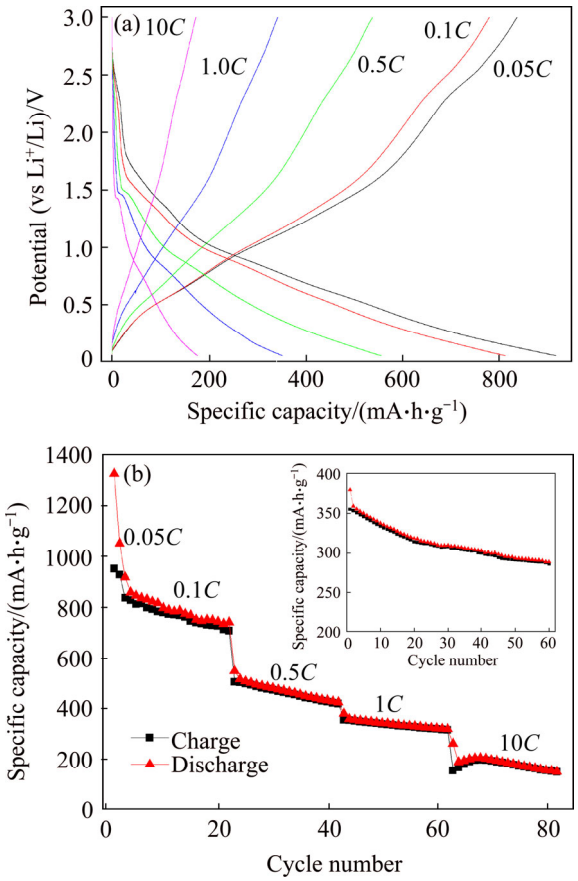

Figure 12 Second cycle galvanostatic discharge−charge curves of $Ce_2Sn_2O_7$ nanocubes at different current densities (a), rate capability at different current densities (b), and correspnelling cycling performance of nanocubes at a current density of 1*C* (b) (Here 1*C* is defined as 994 mA·h/g)

1*C* and 10*C* is 918, 813, 556, 352, and 176 mA·h/g, respectively. Herein, 1*C* arises from the theoretical capacity 994 mA·h/g of Sn. These capacity values are superior as compared with the traditional anode of graphite (about 375 mA·h/g). Figure 12(b) shows the capacity at different current density. As reference with the specific capacity at 0.05*C*, the capacity retention ratio at the current density of 0.1*C*, 0.5*C*, 1*C* and 10*C* is 88.6%, 60.6%, 38.3% and 19.2%, respectively. It demonstrates a remarkable rate capability since this is pristine sample and there is no carbon coating and no introducing of secondary conductive components. The cycling performance of $Ce_2Sn_2O_7$ nanoparticles electrode at a current density of 1*C* is shown in the inset of Figure 12(b). The reversible capacity beyond 60 cycles was maintained at about 286 mA·h/g. The capacity keeps decreasing during the first 10 cycles but becomes pretty stable with a value of about 300 mA·h/g, henceforth from the 10th cycle.

The reaction mechanism is based on reversible intercalation/deintercalation of lithium ions into host structures or lithium alloying reactions, which can be described by the following equation:

$$Ce_2Sn_2O_7+6Li^++6e\leftrightarrow 3Li_2O+2Sn+2CeO_2 \quad (8)$$

$$Sn+xLi^++xe\leftrightarrow Li_xSn \quad (9)$$

The cycle voltammograms of the $Ce_2Sn_2O_7$ electrode for the first three cycles are shown in Figure 13. The CV curves of the three cycles are similar. There is a broad peak at 0.60 V in the first anodic progress, which could be associated with the reduction of Sn^{4+} to Sn^0 and formation of Li−Sn alloys as well as an irreversible reaction related to the decomposition of the electrolyte. During the cathodic process, a peak is presented at 0.70 V, which is associated with the oxidation of Ce^0 to Ce^{4+} and the dealloying of Li−Sn.

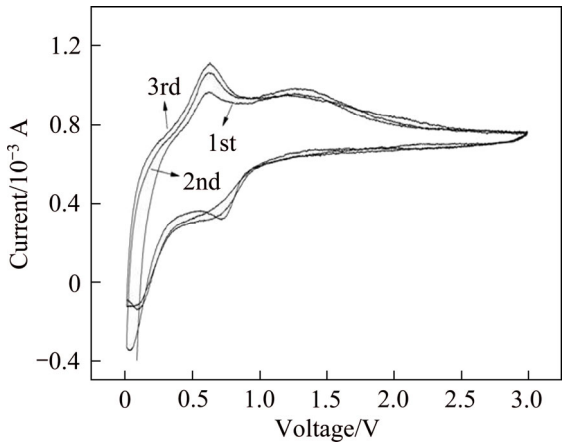

Figure 13 Cycle voltammograms plots of $Ce_2Sn_2O_7$ electrode at scan rate of 0.1 mV/s in voltage range of 0.01−3.00 V

4 Conclusions

A simple hydrothermal strategy has been employed to fabricate ultrafine cube-shape $Ce_2Sn_2O_7$ nanoparticles with a size of about 10 nm and with pure fluorite phase. To obtain single fluorite phase $Ce_2Sn_2O_7$, the optimized conditions were: 180 °C, pH=12, 8 h, using NaOH as precipitator. The pseudo-capacitance properties of the as-synthesized fluorite $Ce_2Sn_2O_7$ nanocube are studied for the first time. The $Ce_2Sn_2O_7$ electrode shows a specific capacitance of 222 F/g when cycled at a constant current density of 100 mA/g. The $Ce_2Sn_2O_7$ electrode also exhibits remarkable cycling stability, after 5000 cycle tests，86% of the original value is maintained. Meanwhile, the obtained $Ce_2Sn_2O_7$ ultrafine nanocubes also have been evaluated as the anode material for lithium ion batteries for the first time. It demonstrates promising electrochemical performance with a good combination of high specific capacity and stable cycling properties. As a result, the as-obtained ultrafine $Ce_2Sn_2O_7$ nanocubes show attractive application as electrode materials for supercapacitors and lithium ion batteries as well.

References

[1] CONWAY B E, PELL W G. Double-layer and pseudocapacitance types of electrochemical capacitors and their applications to the development of hybrid devices [J]. Journal of Solid State Electrochemistry, 2003, 7(9): 637−644.

[2] HU J, LI M C, LV F C, YANY M Y, TAO P P, TANG Y G, LIU H T, LU Z G. Heterogeneous $NiCo_2O_4$@polypyrrole core/sheath nanowire arrays on Ni foam for high performance supercapacitors [J]. Journal of Power Sources, 2015, 294: 120−127.

[3] SIMON P, GOGOTSI Y. Materials for electrochemical capacitors [J]. Nature Materials, 2008, 7: 845−854.

[4] CHENG H, LU Z G, DENG J Q, CHUNG C Y, ZHANG K L, LI Y Y. A facile method to improve the high rate capability of Co_3O_4 nanowire array electrodes [J]. Nano Research, 2010, 3: 895−901.

[5] LIAN J, WANG L M, WANG S X, CHEN J, BOATNER L A,

EWING R C. Nanoscale manipulation of pyrochlore: New nanocomposite ionic conductors [J]. Physical Review Letters, 2001, 87: 145901.

[6] ZHAO J H, KUNKEL H P, ZHOU X Z, WILLIAMS G W, SUBRAMANIAN M A. Critical behavior of the magnetoresistive pyrochlore $Tl_2Mn_2O_7$ [J]. Physical Review Letters, 1999, 83: 219−222.

[7] LUTIQUE S, KONINGS R J M, RONDINELLA V V, SOMERS J, WISS T. The thermal conductivity of $Nd_2Zr_2O_7$ pyrochlore and the thermal behaviour of pyrochlore-based inert matrix fuel [J]. Journal of Alloys and Compounds, 2003, 352: 1−5.

[8] NAG A, DASGUPTA P, JANA Y M, GHOSH D. A study on crystal field effect and single ion anisotropy in pyrochlore europium titanate ($Eu_2Ti_2O_7$) [J]. Journal of Alloys and Compounds, 2004, 384: 6−11.

[9] SOHN J M, KIM M R, WOO S I. The catalytic activity and surface characterization of $Ln_2B_2O_7$ (Ln=Sm, Eu, Gd and Tb; B=Ti or Zr) with pyrochlore structure as novel CH_4 combustion catalyst [J]. Catalysis Today, 2003, 83: 289−297.

[10] ALI N, HILL P, ZHANG X, WILLIS F. Magnetization and thermoremanent magnetization of $Tb_2Mo_2O_7$ and $Y_2Mo_2O_7$ spin glasses [J]. Journal of Alloys and Compounds, 1992, 181: 281−285.

[11] YANG M Y, CHENG H, GU Y Y, SUN Z F, HU J, CAO L J, LV F C, LI M C, WANG W X, WANG Z Y, WU S F, LIU H T, LU Z G. Facile electro-deposition of 3D concentration-gradient Ni-Co hydroxide nanostructures on nickel foam as high performance electrodes for asymmetric supercapacitors [J]. Nano Research, 2015, 8(8): 2744−2754.

[12] SHARMA N, SUBBA R G V, CHOWDARI B V R. Anodic properties of tin oxides with pyrochlore structure for lithium ion batteries [J]. Journal of Power Sources, 2006, 159: 340−344.

[13] MIMS C A, JACOBSON A J, HALL R B, LEWANDOSKI J T. Methane oxidative coupling over nonstoichiometric bismuth-tin pyrochlore catalysts [J]. Journal of Catalysis, 1995, 153: 197−207.

[14] CHENG H, WANG L P, LU Z G. A general aqueous sol–gel route to $Ln_2Sn_2O_7$ nanocrystals [J]. Nanotechnology, 2008, 19: 025706.

[15] YU T H, TULLER H L. Ionic conduction and disorder in the $Gd_2Sn_2O_7$ pyrochlore system [J]. Solid State Ionics, 1996, 86−88: 177−182.

[16] PORAT O, HEREMANS C, TULLER H L. Stability and mixed ionic electronic conduction in $Gd_2(Ti_{1-x}Mo_x)_2O_7$ under anodic conditions [J]. Solid State Ionics, 1997, 94: 75−83.

[17] SICKAFUS K E, MINERVINI L, GRIMES R W, VALDEZ J A, ISHIMARU M, LI F, MCCLELLAN K J, HARTMANN T. Radiation tolerance of complex oxides [J]. Science, 2000, 289: 748−751.

[18] LI K W, WANG H, HUI Y. Hydrothermal preparation and photocatalytic properties of $Y_2Sn_2O_7$ nanocrystals [J]. Journal of Molecular Catalysis A: Chemical, 2006, 249: 65−70.

[19] TOLLA B, DEMOURGUES A, POUCHARD M, RABARAEL L, FOURNES L, WATTIAUX A. Oxygen exchange properties in the new pyrochlore solid solution $Ce_2Sn_2O_7$-$Ce_2Sn_2O_8$ [J]. Comptes Rendus de l' Academie des Sciences Serie IIc: Chemie, 1999, 2: 139−146.

[20] ISMUMANDAR KENNEDY B J, HUNTER B A, VOGT T. Bonding and structural variations in doped $Bi_2Sn_2O_7$ [J]. Journal of Solid State Chemistry, 1997, 131: 317−325.

[21] WANG S W, LU M K, ZHOU G J, ZHOU Y Y, ZHANG H P, WANG S F, YANG Z S. Synthesis and luminescence properties of $La_{2-x}RExSn_2O_7$ (RE=Eu and Dy) Phosphor nanoparticles [J]. Materials Science and Engineering: B, 2006, 133: 231−234.

[22] MOON J, AWANO M, MAEDA K. Hydrothermal synthesis and formation mechanisms of lanthanum tin pyrochlore oxide [J]. Journal of the American Ceramic Society, 2001, 84: 2531−2536.

[23] LU Z G, WANG J W, TANG Y G, LI Y D. Synthesis and photoluminescence of Eu^{3+}-doped $Y_2Sn_2O_7$ nanocrystals [J]. Journal of Solid State Chemistry, 2004, 177: 3075−3079.

[24] ZHU H L, JIN D L, ZHU L M, YANG H, YAO K H, XI Z Q. A General hydrothermal route to synthesis of nanocrystalline lanthanide stannates: $Ln_2Sn_2O_7$ (Ln=Y, La-Yb) [J]. Journal of Alloys and Compounds, 2008, 464: 508−513.

[25] ZENG J, WANG H, ZHANG Y C, ZHU M K, YAN H. Hydrothermal synthesis and photocatalytic properties of pyrochlore $La_2Sn_2O_7$ nanocubes [J]. Journal of Physical Chemistry C, 2007, 111: 11879−11887.

[26] HUANG H, MIAO X, LIAO N, WANG L C, JIN D L. Study on the oxygen exchange capacities of $Ce_2Sn_2O_7$ pyrochlore [J]. Russian Journal of Inorganic Chemistry, 2011, 56: 1621−1624.

[27] YANG J Y, SU Y C, LIU X Y. Hydrothermal synthesis, characterization and optical properties of $La_2Sn_2O_7$: Eu^{3+} micro-octahedra [J]. Transactions of Nonferrous Metals Society of China, 2011, 21: 535−543.

[28] GLERUP M, NIDLSEN O F, POULSEN F W. The structural transformation from the pyrochlore structure, $A_2B_2O_7$, to the fluorite structure, AO_2, studied by Raman spectroscopy and defect chemistry modeling [J]. Journal of Solid State Chemistry, 2001, 160: 25−32.

[29] WU S F, WANG W X, Li M C, CAO L J, LV F C, YANG M Y, WANG Z Y, SHI Y, NAN B, YU S C, SUN Z F, LIU Y, LU Z G. Highly durable organic electrode for sodium-ion batteries via a stabilized α-C radical intermediate [J]. Nature Communications, 2016, 7: 13318.

[30] GUPTA H C, BROWN S, RANI N, GOHEL V B. A lattice dynamical investigation of the Raman and the infrared frequencies of the cubic $A_2Sn_2O_7$ pyrochlores [J]. International Journal of Inorganic Materials, 2001, 3: 983−986.

[31] VANDENBORRE M T, HUSSON E, CHATRY J P, MICHEL D. Rare-earth titanates and stannates of pyrochlore structure; vibrational spectra and force fields [J]. Journal of Raman Spectroscopy, 1983, 14: 63−71.

[32] XU M W, KONG L B, ZHOU W J, LI H L. Hydrothermal synthesis and pseudocapacitance properties of α-MnO_2 hollow spheres and hollow urchins [J]. The Journal of

Physical Chemistry C, 2007, 111: 19141−19147.
[33] TOUPIN M, BROUSSE T, BELANGER D. Charge storage mechanism of MnO_2 electrode used in aqueous electrochemical capacitor [J]. Chemistry of Materials, 2004, 16: 3184−3190.
[34] LI F H, SONG J F, YANG H F, GAN S Y, ZHANG Q X, HAN D X, ARILVASKA LI N. One-step synthesis of Graphene/SnO_2 nanocomposites and its application in electrochemical supercapacitors [J]. Nanotechnology, 2009, 20: 455602.
[35] PANG S C, ANDERSON M A, CHAPMAN T W. Novel electrode materials for thin-film ultracapacitors: Comparison of electrochemical properties of sol-gel-derived and electrodeposited manganese dioxide [J]. Journal of the Electrochemical Society, 2000, 147: 444−450.
[36] SUBRAMANIAN V, ZHU H W, VAJTAI R, AJAYAN P M, WEI B Q. Hydrothermal synthesis and pseudocapacitance properties of MnO_2 nanostructures [J]. The Journal of Physical Chemistry B, 2005, 109: 20207−20214.
[37] LEE H Y, GOODENOUGH J B. Supercapacitor behavior with KCl electrolyte [J]. Journal of Solid State Chemistry, 1999, 144: 220−223.

(Edited by FANG Jing-hua)

中文导读

超细 $Ce_2Sn_2O_7$ 纳米立方晶体的水热合成与储能性能

摘要：采用简单水热法合成了尺寸为 10 nm 左右的纯烧绿石相超细 $Ce_2Sn_2O_7$ 立方晶体。通过优化温度、pH、反应时间、前驱体类型等参数获得最佳实验条件。通过 X 射线衍射仪、拉曼光谱、透射电子显微镜、高分辨透射电子显微镜和 BET 等表征技术对样品的晶体结构、形貌、尺寸和比表面积进行表征。将制备的 $Ce_2Sn_2O_7$ 超细纳米立方晶体用作电极材料，并通过超级电容器和锂离子电池对其性能进行评估。将其应用于超级电容器，在 0.1 A/g 下具有 222 F/g 的高比电容，并且在 5000 次循环后仍具有良好的循环稳定性，电容保持率高于 86%。将其用于锂离子电池负极材料时，在 0.05*C* 倍率下具有超过 900 mA·h/g 的高电池容量。与传统的石墨阳极相比，其倍率性能和循环性能呈现出较好的应用前景。

关键词：超级电容器；锂离子电池；复合氧化物；超细纳米晶；水热法；烧绿石